

Ab-initio study of quantum oscillation in altermagnetic and nonmagnetic phases of RuO₂

Yingliang Huang,^{1,2} Junwen Lai,^{1,2} Jie Zhan,^{1,2} Tianye Yu,² Rong Chen,^{2,3} Peitao Liu,^{1,2} Xing-Qiu Chen,^{1,2,*} and Yan Sun^{1,2,†}

¹School of Materials Science and Engineering, University of Science and Technology of China, Shenyang 110016, China

²Shenyang National Laboratory for Materials Science, Institute of Metal Research, Chinese Academy of Sciences, Shenyang 110016, China

³School of Materials Science and Engineering, Northeastern University, Shenyang 110819, China

E-mail: xingqiu.chen@imr.ac.cn; sunyan@imr.ac.cn

Abstract

Altermagnet (AM) is a new proposed magnetic state with collinear antiferromagnetic ground state but presents some transport properties that were only believed to exist in ferromagnets or non-collinear antiferromagnets. To have a comprehensive understanding of the transport properties of AMs, especially from the experimental point of view, a promising altermagnetic metal is crucial. In all the proposed altermagnetic metals, RuO₂ has a special position, since it is the first proposed AM with the largest spin splitting and several important altermagnetism featured experiments were first performed based on it. However, a very recent report based on sensitive muon-spin measurements suggest a super small local magnetization from Ru, i.e. a nonmagnetic ground state in RuO₂. Therefore, a determination of the existence of the altermagnetic ground state is the basic starting point for all the previously altermagnetic transport properties in RuO₂. In this work, we propose to identify its magnetic ground state from the Fermi surface (FS) via the electronic transport property of quantum oscillation (QO). We systematically analyzed the FSs of RuO₂ in both nonmagnetic and altermagnetic states via first principles calculations. Our work should be helpful for future experiments on QO measurements to confirm its ground state by the interplay between transport measurements and computations.

I. BACKGROUND AND INTRODUCTION

In traditional understanding, the collinear magnetic ordered state can be classified into ferromagnet (FM) and antiferromagnet (AFM) according to their ground state and exchange energies. Very recently, the understanding of collinear AFMs was refreshed and a new magnetic state of altermagnet (AM) was proposed from the symmetry points of view[1-7]. Different from traditional AFM with two sublattices connected by time-reversal and translation/inversion[8], the AM follows the rotation symmetry. With the special symmetry, the AM presents as AFM in energy ground state and FM-like spin split in electronic band structure[9-12]. Owing to the spin split, the AM hosts some special transport properties that were only believed to exist in FM and non-collinear AFMs, such as anomalous Hall effect[13-16], non-SOC spin current[17], magneto-optical responses[18], and C-paired spin-valley locking[19,20], etc. The joint advantages of FM-like transport and AFM-like ground state in AM open a new avenue for magnetic-based applications of message processing, data storage and even quantum computing, etc[21-24].

To have a comprehensive understanding of AM-related properties, realistic materials are desired for both materials computations and experimental measurements. With the concept in mind, many AM materials were theoretically proposed and some of them were experimentally verified[11,12,14,15,21-23,25-28]. In all these AMs, Rutile RuO₂ has a special position, since it was the first proposed AM with the largest spin split up to 1.4 eV[2]. So far, most of the interesting phenomena in AMs were carried by electron currents, which make realistic AM metals especially important and most related measurements were performed based on RuO₂. The collinear AFM magnetic structure in RuO₂ was identified based on the measurements of resonant X-ray scattering and neutron diffraction[29,30]. According to these reports,

the two sublattices of Ru are connected by a four-fold screw rotation operation, belonging to the AM classification.

Very recently, a systematic study of the magnetic structure in RuO₂ single crystal was carried out via a local moment-sensitive measurement of muon spin rotation and relaxation (μ SR) [31]. According to the new measurements, the local magnetic moment on each Ru site is in the order of 10^{-4} μ B, much smaller than the previous reports and AM requirements[30]. So, it can be considered as a nonmagnetic or paramagnetic ground state. It proposed that the previously reported and alleged magnetic reflections are likely related to multiple scattering artifacts rather than to a magnetic origin[32]. The conflicting evidence from different measurements motivated the research community to look back at all the AM-related transport properties in RuO₂. Therefore, it is crucial to have a clear and definitive understanding of its magnetic ground state. In this work we propose a strategy to identify the magnetic ground state based on the magneto-transport properties of quantum oscillation (QO). Recently, a systematic theoretical study of the QO for altermagnet were reported based on effective model analysis[33]. The big difference between the Fermi surfaces (FSs) in altermagnetic and nonmagnetic states of RuO₂ will lead to significant differences in the QO signals, which can be utilized as a powerful tool to understand the magnetic ground state[34].

II. METHOD

The electronic structure calculations for RuO₂ were performed using the Vienna Ab initio Simulation Package (VASP)[35] with the Generalized Gradient Approximation (GGA) as formulated by Perdew, Burke, and Ernzerhof (PBE)[36]. The plane-wave basis set was employed with a kinetic energy cutoff of 500 eV to ensure the accuracy of the results. For the AM state calculations, a Hubbard U of 2 eV was applied, as previous DFT calculations and experimental measurements have shown that the magnetic moment and anomalous Hall conductivity (AHC) are best matched with experimental values when $U = 2$ eV[14,29,30,37,38]. After obtaining the converged electronic structure from VASP, we performed maximally localized Wannier function (MLWF) projection to construct the tight-binding Hamiltonians[39]. The Wannier functions were generated to represent the Ru d-orbitals and O p-orbitals, providing a detailed and accurate description of the electronic states near the Fermi level. Using the constructed tight-binding Hamiltonian, we calculated the extreme cross-sectional areas of the FSs. The Onsager relation[40], $F = (\frac{h}{2\pi e})S_f$, was then employed to determine the QO frequencies (F). Oxygen defects are an inherent issue in transition metal oxides. Their presence introduces additional electrons, thereby elevating the Fermi level, which leads to slight changes in the quantum oscillation signals. Oxygen defects also act as scattering centers, reducing the mean free path of electrons, which can result in certain cyclotron orbits being undetectable in experiments. However, the overall structure of the Fermi surface and the fundamental characteristics of the magnetic ground state remain largely unaffected. So in this work, we considered the clean and low temperature approximations.

III. RESULTS AND DISCUSSION

RuO₂ exhibits a rutile-type crystal structure, belonging to the space group $P4_2/mnm$ (No. 136). In this structure, each Ru atom is surrounded by six O atoms, forming an octahedron with two-fold rotational symmetry. The crystal structure and magnetic structure are illustrated in Fig. 1(a) and (b), respectively. The potential magnetic moments are located on the Ru sites, originating from the 4d orbitals, with the easy axis along the [001] direction[30,41].

To investigate the differences between nonmagnetic and altermagnetic states of RuO₂, the FSs of both magnetic states are calculated, see Fig. 1(c-d). In the nonmagnetic state, there are three independent FS bubbles. The first one is close to the $k_z = \pm\pi/c$ plane (with label FS1), the second one is approximately spherical around the Γ point (with label FS2), and the third one is a small bubble located around the hinge of Brillouin zone (BZ) $k_x = k_y = \pm\pi/a$ (with label FS3). After taking the magnetic order into consideration with including on-site $U=2$ eV, the FSs change dramatically. As presented in Fig. 1(d), we plot the spin-up and spin-down channels connected by a S_{4z} screw rotation symmetry in different colors. The magnetic RuO₂ FSs consist of three major parts: two intersecting semi-ellipsoids at the top and bottom of the BZ, FSs located at the four corners near $k_z = 0$, and a d_{xy} -orbital-like closed structure around the Γ point. The dramatic differences of FSs in the two possible magnetic states enable us to use the QO to identify the true ground states in experiments.

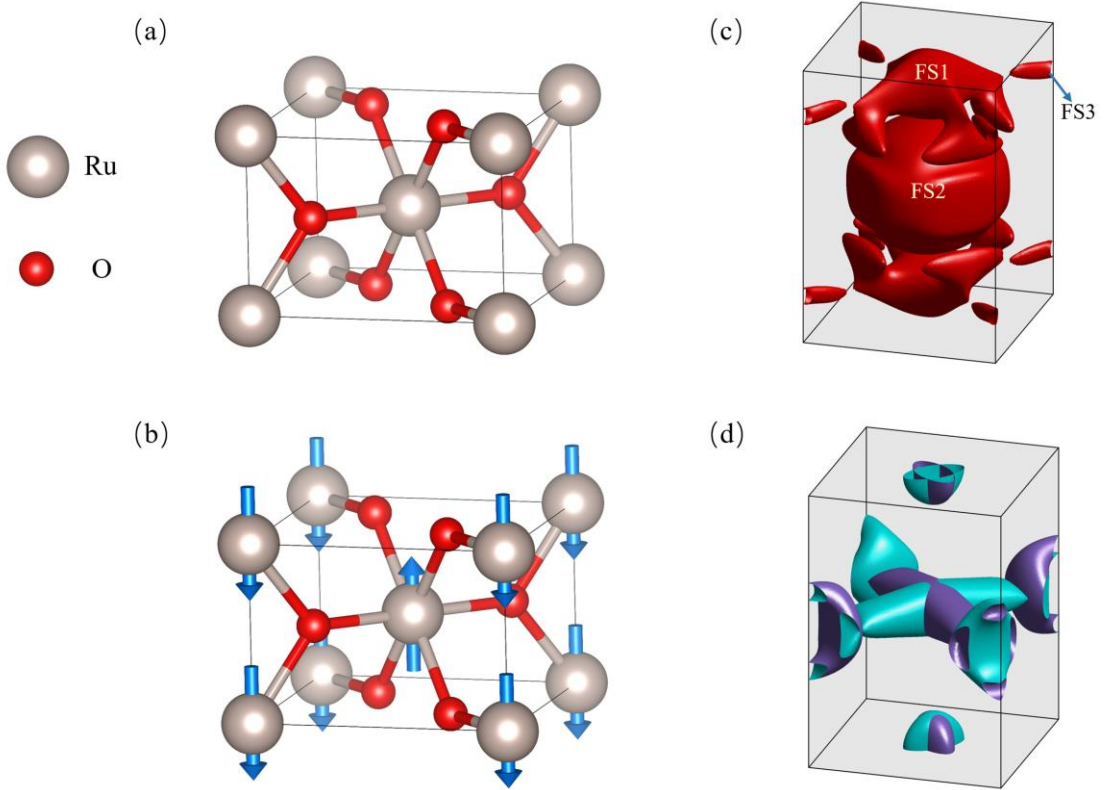


FIG.1. Crystal structure and Fermi surface (FS) of RuO₂. (a) Crystal structure of nonmagnetic RuO₂. (b) Crystal and magnetic structure of altermagnetic RuO₂. (c) FS of nonmagnetic RuO₂ with the consideration of spin-orbital coupling (SOC). (d) FS of altermagnetic RuO₂ without the consideration of SOC.

The difference between nonmagnetic and AM states can also be seen from electronic band structures, as presented in Fig. 2. From Fig. 2(b) one can see that the bands cutting Fermi level mainly happen around Γ points, on the line of Γ -X, Γ -M and Γ -Z. In addition, there is a small Fermi cutting on the line of A-M close to point A, fully consistent with the FS in Fig. 1(c). With the consideration of spin-orbital coupling (SOC), some degeneracy on Γ -Z, R-Z, and R-A are broken but just with small spin splittings, due to weak SOC induced the $SU(2)$ symmetry breaking. After taking magnetic order into consideration, the electronic band structure changes completely, and a large spin split around 1.4eV can be found in the M- Γ direction near the Fermi level, see Fig. 2(c), fully consistent with previous reports[2]. Similar to the

case without adding on-site U , some new band splittings are generated by the SOC effect, which leads to a visible dispersion of the original flat band in the spin-down channel along $M-\Gamma$. Owing to the changes of energy dispersions after considering the magnetic moment, the Fermi cutting also changes a lot. In comparison to the case without magnetism, the distances from Fermi cutting to Γ become very different on the $\Gamma-X$, $\Gamma-M$, and $\Gamma-Z$, leading to a d_{xy} -orbital-like flat FS around Γ points. Besides, one new small FS is formed around the M point for each spin channel.

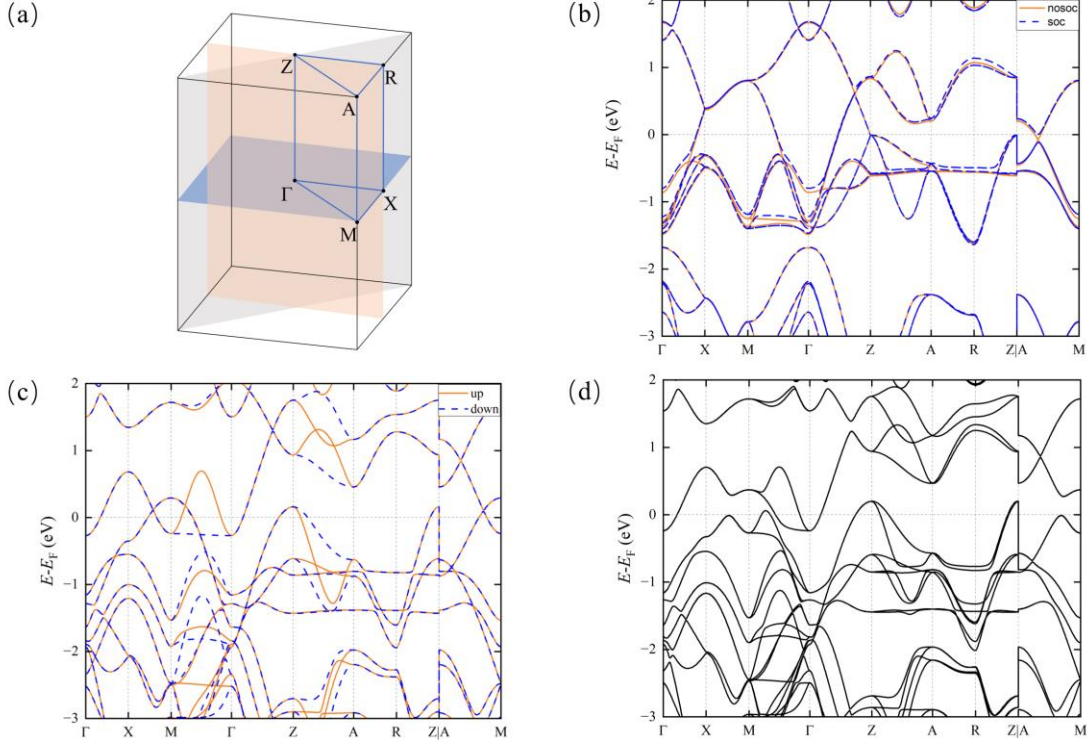


FIG.2. The Brillouin zone (BZ) and band structure of RuO₂. (a) The three-dimensional BZ of RuO₂, with the blue plane representing the [001] plane, the orange plane representing the [100] plane, and the gray plane representing the [110] plane. (b) Band structure of nonmagnetic RuO₂ without considering SOC and with considering SOC, respectively. (c) Band Structure of altermagnetic RuO₂ without considering SOC (orange solid line for spin up, the blue dash for spin down). (d) Band Structure of altermagnetic RuO₂ with considering SOC.

To simulate the QO in magneto-transport signals, we adopted an angular rotation strategy to provide as many characteristic curves of QO frequencies as possible, thereby offering more robust evidence for diagnosing the presence of magnetism through QO measurements. The rotation angles span from the [001] direction to the [100] direction by 90°, then from the [100] direction to the [110] direction by 45°, and finally from the [110] direction back to the [001] direction by 90°. This extensive angular range allows us to collect nearly comprehensive QO frequency data, providing a thorough basis for our analysis. Though the ground state can be understood without considering SOC, SOC always exists in practical materials, and its effect is not small in a 4d-orbital dominated FS here. So, in all the QO calculations, we included the SOC effect.

Fig. 3(a) shows the angle-dependent QO frequencies of nonmagnetic RuO₂, derived from the extreme cross-sectional areas of three independent closed FSs. The evolution of the angle-dependent QO contributed from FS1 can be effectively described by 11 typical extreme cross-sections along with the

rotation of the applied magnetic field, as shown in Fig. 3(b).

Initially, as the magnetic field rotates from the [001] direction to the [100] direction in the range of 0° to $\sim 24^\circ$, two maximums appear at the front legs of FS1, corresponding to the FS1-cut1 curve. After 24° , no extreme value exists anymore. Though FS1 follows the four-fold rotation symmetry, the contribution from different legs of this FS is different when we rotate the magnetic field from [001] to [100]. The contribution of the other two legs can survive in a relatively large range of 0° to $\sim 60^\circ$. So, we can see that the four legs of FS1 correspond to frequencies close to 900T with magnetic field rotating from [001] to [100], see the left lower corner in Fig. 3(a). Following FS1-cut1 at the angle of $\sim 24^\circ$, further rotating the magnetic field, a new cross section appears, see the FS1-cut3 in Fig. 3(b). This extreme cross section can exist in a large range of $\sim 25^\circ$ to 90° and can even exist in a small range of 25° to $\sim 6^\circ$ in the other rotation direction from [100] to [110]. The extreme cross section of FS1-cut3 can contribute to a large Frequency window in the range of $\sim 2400\text{T}$ to $\sim 4600\text{T}$, see the label on the left part of Fig. 3(a).

When we rotate the magnetic field to $\sim 75^\circ$, a new extreme cross section appears, see FS1-cut4 in Fig. 3(b). Similar to the case in FS1-cut3, the extreme cross section from FS1-cut4 can also exist in the two rotation directions from [001] to [100] and from [100] to [110], with the frequencies in a range of $\sim 2100\text{T}$ to $\sim 2700\text{T}$, see the corresponding label in Fig. 3(a). Around the [110] direction, a large extreme area involving two nearby legs and the head of FS1 appears, see FS1-cut5 in Fig. 3(b). It can survive in the range up to $\sim 15^\circ$ and $\sim 70^\circ$ with rotating magnetic field away from [110] to [100] and [001], respectively, with frequencies in the range of $\sim 3600\text{T}$ to $\sim 4700\text{T}$. The front right leg of FS1 can generate another effective cutting as FS1-cut6 with frequencies near $\sim 1000\text{T}$ when the magnetic field is rotating between [100] and [110] directions.

A smaller section from FS1-cut7 represents the connection between the front right leg and the head, see Fig. 3(b). As rotation passes the [110] direction and continues towards the [001] direction, FS1-cut7 evolves into two parts, with FS1-cut8 from the rear left leg and head connection and FS1-cut9 from the front right leg and head connection. These two minimums exhibit entirely different trends with rotation, where FS1-cut9 increases sharply from $\sim 400\text{T}$ to $\sim 1800\text{T}$ and FS1-cut8 remains almost constant near $\sim 300\text{T}$.

Similarly, as rotation passes the [110] direction and continues towards the [001] direction, FS1-cut6 evolves into two parts, with FS1-cut10 from the rear left leg and FS1-cut11 from the front right leg. These two maximums also exhibit different trends with rotation, where FS1-cut10 increases sharply from $\sim 1400\text{T}$ to $\sim 3000\text{T}$ and FS1-cut11 decreases from $\sim 1400\text{T}$ to $\sim 900\text{T}$.

In comparison to FS1, the shape of FS2 is much simpler in a form that's almost spherical. So, the corresponding evolution of frequencies along with rotation is continuous in all the checked directions and confined in the range of $\sim 8500\text{T}$ to $\sim 10300\text{T}$, as presented in the top part of Fig. 3(a). In addition, there is also a very small FS3 located around the corner of BZ with a "cross-like" shape, see Fig.3 (d). Frequency evolution of FS3 is also continuous in all the checked directions, as presented at the bottom of Fig. 3(a). The extreme cross-sectional area corresponding to FS3-cut ranges from $\sim 100\text{T}$ to $\sim 800\text{T}$, with the continuous evolution of frequency across the whole angle.

Fig. 4(a) shows the angle-dependent QO frequencies of AM phase RuO_2 , with the magnetic field rotated through the same angles as in the nonmagnetic case. There are five independent FS bubbles in total, as presented in Fig. 4(b). The extreme cross-sections of the magnetic RuO_2 FSs (FS1-FS4) are relatively simpler and more straightforward due to their convex FS, exhibiting continuous evolution throughout the rotation. FS1-cut has its smallest extreme cross-section along the [001] direction,

gradually reaching its maximum as it rotates to [100] direction, with continuous frequencies in the range of $\sim 700\text{T}$ to $\sim 1400\text{T}$. FS2-cut has a nearly square minimum cross-section in the [001] direction and reaches its maximum when rotated to the [100] direction, with frequencies in the range of $\sim 1000\text{T}$ to $\sim 1400\text{T}$. FS3-cut reaches a minimum at the [100] direction and a maximum at the [110] direction with frequencies in the range of $\sim 1500\text{T}$ to $\sim 2000\text{T}$. FS4-cut has an "x"-shaped cross-section along the [001] direction, corresponding to the maximum QO frequency $\sim 6000\text{T}$. When rotated to the [100] direction, FS4-cut reaches a frequency minimum at $\sim 1700\text{T}$.

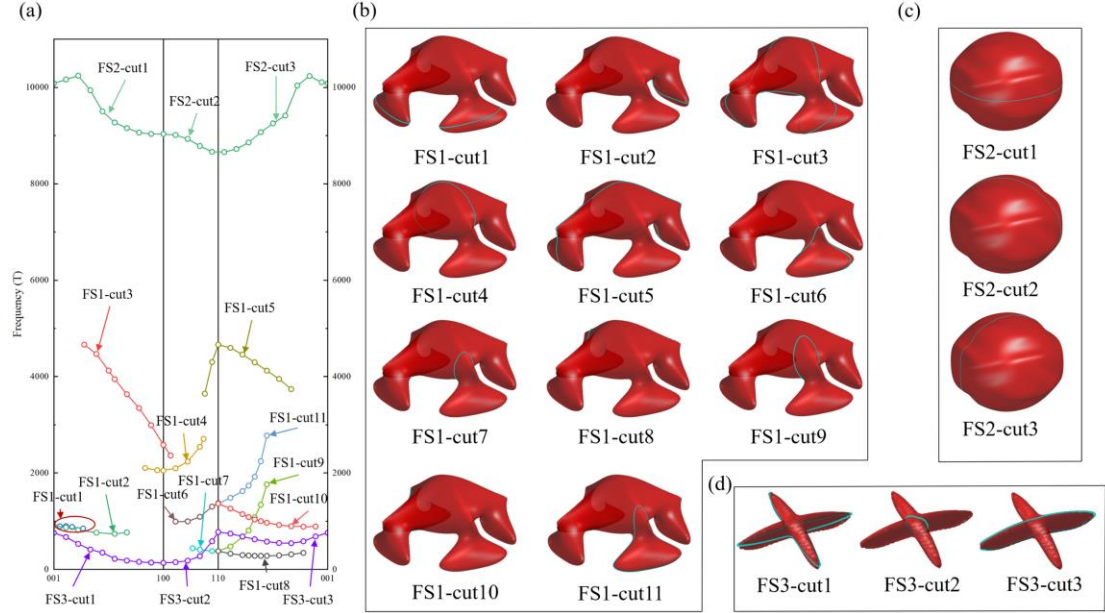


FIG.3. The angle-dependent quantum oscillation (QO) of RuO_2 in nonmagnetic phase and the cross-sectional extreme value details. (a) Angle-dependent QO frequency with applied magnetic field changing from [001] to [100], [100] to [110], and finally from [110] back to [001]. (b-d) Typical extreme cross-sectional areas in FS1, FS2, and FS3.

FS5 is relatively complicated and has three distinct extreme cross-sections. As the magnetic field rotates from the [001] direction to the [100] direction in the range of $\sim 60^\circ$ to $\sim 75^\circ$, two maximums appear in FS5, corresponding to the curve of FS5-cut1 in Fig.4(b). After $\sim 85^\circ$, these two maximums merge to form a new maximum, see FS5-cut2 in Fig. 4(b). This cross section survives in the whole range of [100] to [110] and continues from 0° to $\sim 75^\circ$ from [110] to [001], with frequencies from $\sim 2200\text{T}$ to $\sim 2600\text{T}$. After that, the one big cross section becomes four small maximums, see FS5-cut3 in Fig. 4(b), with frequencies near $\sim 500\text{T}$, see FS5-cut3 in Fig. 4(b).

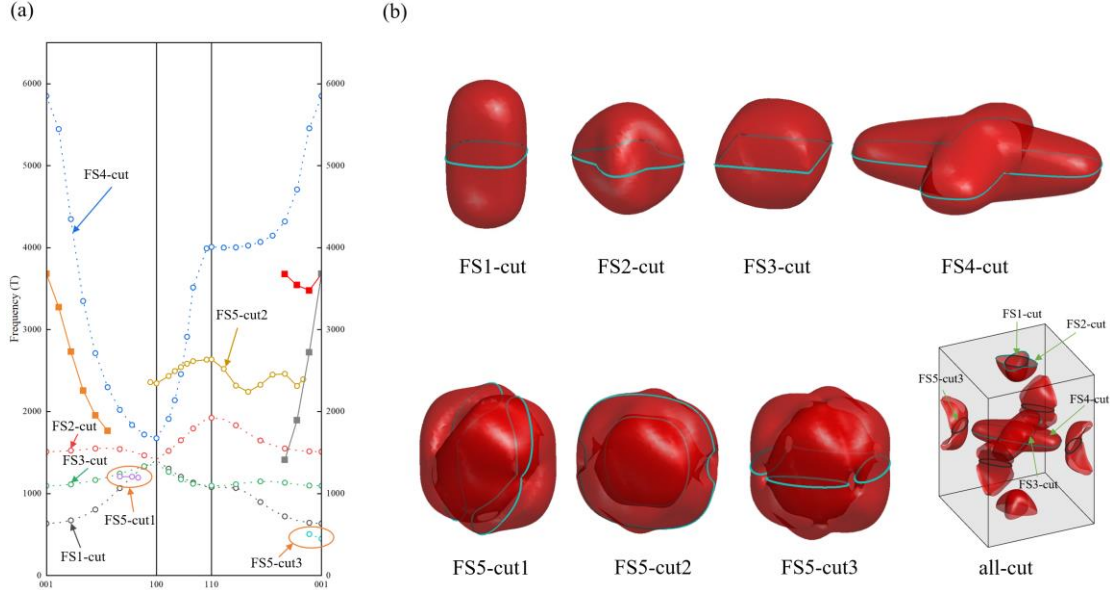


FIG.4. The angle-dependent QO frequencies of altermagnetic RuO_2 and the cross-sectional extreme value details. (a) Angle-dependent QO frequency data. The direction of the applied magnetic field changes from $[001]$ to $[100]$, $[100]$ to $[110]$, and finally from $[110]$ back to $[001]$. (b) Typical extreme cross-sectional areas in FS1-FS5.

We considered the presence of SOC in real materials and further mapped the spin texture for each cross-section of the altermagnetic RuO_2 , as shown in Fig. 5. It can be observed in Fig. 5(a) and Fig. 5(e) that there are sharp spin transitions at certain points, which are generally thought to prevent electrons from smoothly passing through, making it difficult to observe these QO frequencies in experiments. In Fig. 4(a), the QO frequencies corresponding to sharp spin transitions are represented by dotted lines, while those with continuous spin variations are indicated by solid lines.

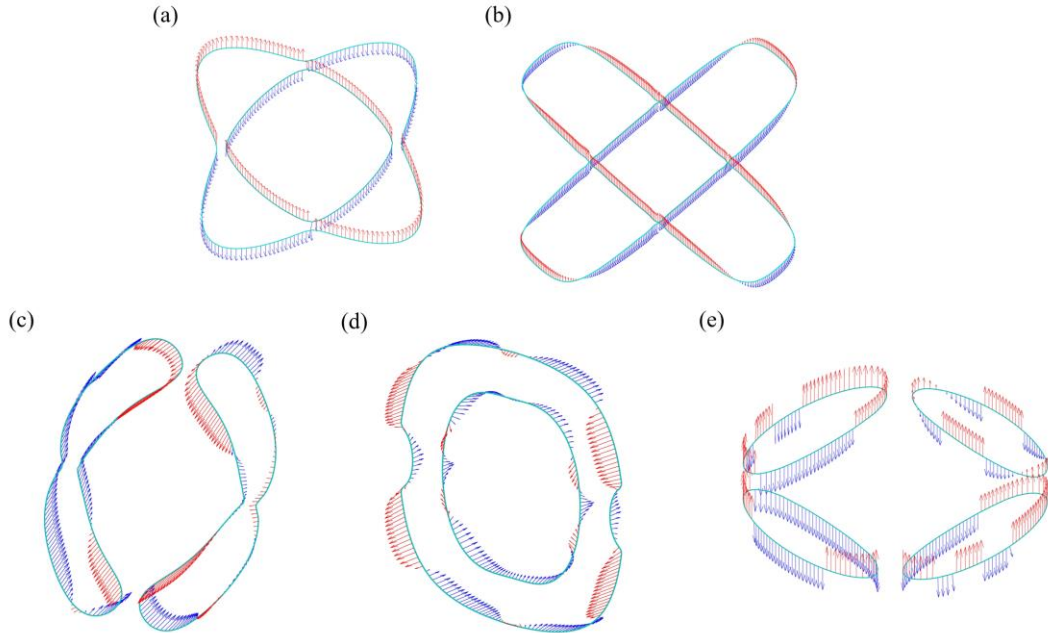


FIG.5. The spin texture of various cross-sections corresponding to the altermagnetic RuO_2 . (a) Spin texture of FS1-cut and FS2-cut, (b) Spin texture of FS3-cut and FS4-cut, (c-e) Spin texture of FS5 (red represents spin along the positive direction of the cross-section, blue arrows represent spin along the negative direction of the cross-section).

Interestingly, in the [001] direction, FS3 and FS4 exhibit a topological structure of the Fermi surface, where the Fermi surfaces of these two bands touch within the red box. This occurs due to the protection by mirror symmetry. As shown in Fig. 6(b), when an electron initially follows the green trajectory, due to a sharp change in its spin, this trajectory may not be detectable in experiments. Instead, as the electron approaches the nodal point, magnetic breakdown occurs, causing the electron to enter a different orbit, consistent with the principle of continuous spin evolution. This alters the original cyclotron orbit and results in different QO frequencies.

The change of area is illustrated in Fig. 6(c). The top two cross sections show the original electron orbits, while the bottom two are the new orbits after the switch of trajectory. The cross-sectional areas of the original orbits are 0.5581 \AA^{-2} and 0.1044 \AA^{-2} , corresponding to two new areas of 0.3316 \AA^{-2} . This leads to the appearance of new QO frequencies, which are represented by the squares on the left and right parts of Fig. 4(a).

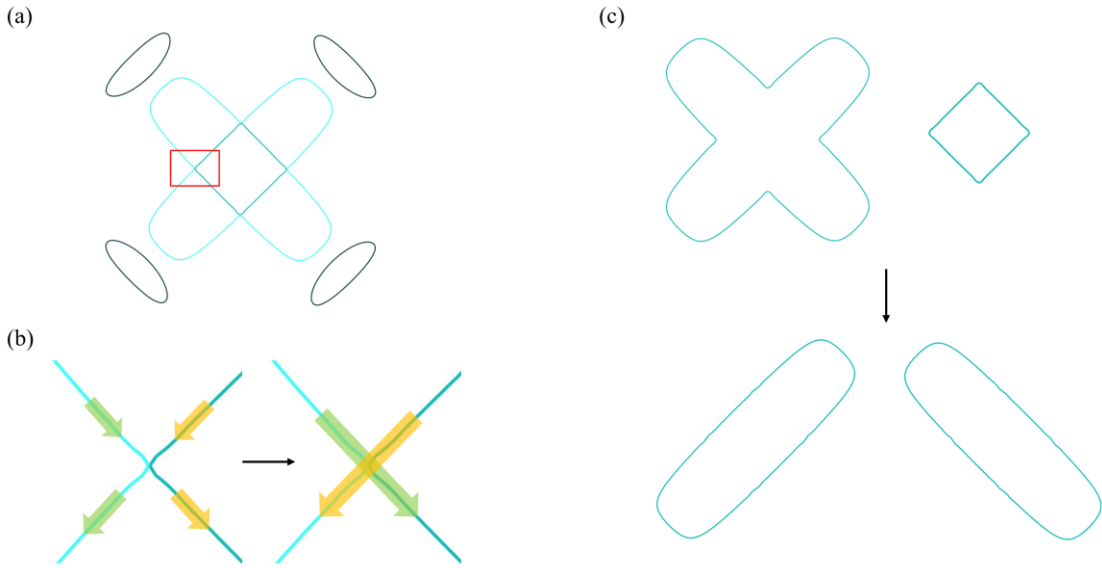


FIG.6. Topological structure of the cross section when magnetic field towards [001] in AM phase. (a) The FS cross section in the BZ when magnetic field towards [001]. The topological structure appears in the red box. (b) The topological structure of the FS changes the trajectory of electron. (c) Different electron cyclotron orbits appear due to the topological structure of the FS.

Due to the topological structure being symmetry-protected, rotating the magnetic field direction causes the separation of the FS contact points. However, because of magnetic breakdown[42,43], when electrons move along cyclotron orbits, they can "tunnel" through small gaps, resulting in new frequencies from complex trajectories[44]. The magnetic breakdown probability occurring when electrons pass through these nodes can be expressed as:

$$P \approx e^{-B_0/B}, \quad \text{where} \quad B_0 = \frac{\hbar k_g^2}{e}$$

where B_0 is the characteristic breakdown field, and B is the applied external magnetic field. The value of B_0 is determined by the breakdown gap k_g between the two trajectories in k-space[45]. Here, \hbar is the reduced Planck constant, and e is the electron charge. Under typical experimental conditions, P ranges between 0 and 1. We performed fine angular adjustments near the [001] direction and found that the

probability of magnetic breakdown gradually decreases with small angular changes, reaching approximately 35% at around 10° . The angle-dependent magnetic breakdown probability is shown in Table I. This phenomenon indicates that the new frequency does not immediately vanish with slight changes in the magnetic field direction even if the symmetry is broken.

TABLE I. This table shows the variation of magnetic breakdown probability with the angle θ in two directions away from [001], under an external magnetic field B of 10T.

[001]-[100] (θ)	1°	2°	3°	4°	6°	8°	10°
$P(B=10T)$	94.0%	91.2%	87.9%	83.0%	70.3%	55.3%	35.0%
[001]-[110] (θ)	1°	2°	3°	4°	6°	8°	10°
$P(B=10T)$	94.7%	93.8%	92.2%	90.7%	86.3%	76.9%	35.9%

IV. SUMMARY

In summary, we have presented a detailed analysis for the QO in the two most promising ground states of nonmagnetic and AM phases. Our calculations show dramatic differences of their FSs and corresponding QO frequency diagrams, which can be easily identified by magneto-transport measurements. We believe that it is sufficient to determine the presence or absence of magnetism in RuO_2 by this method. Moreover, we also found a signature of topological structure in the FS cross-section in the [001] direction of magnetic RuO_2 . This symmetry-protected nodal line band structure can lead to some new electron trajectories and QO frequencies, which can serve as another important feature for the identification.

ACKNOWLEDGMENTS

This work was supported by the National Key R&D Program of China 2021YFB3501503, National Natural Science Foundation of China (Grants No.52271016, No.52188101), and Liaoning Province (Grant No. XLYC2203080). Part of the numerical calculations in this study were carried out on the ORISE Supercomputer (No. DFZX202319).

References

- [1] I. I. Mazin, Altermagnetism-A New Punch Line of Fundamental Magnetism, *Phys. Rev. X* **12**, 040002 (2022).
- [2] L. Smejkal, J. Sinova, and T. Jungwirth, Emerging Research Landscape of Altermagnetism, *Phys. Rev. X* **12**, 040501 (2022).
- [3] L. Smejkal, J. Sinova, and T. Jungwirth, Beyond Conventional Ferromagnetism and Antiferromagnetism: A Phase with Nonrelativistic Spin and Crystal Rotation Symmetry, *Phys. Rev. X* **12**, 031042 (2022).
- [4] P. A. McClarty and J. G. Rau, Landau Theory of Altermagnetism, *Phys. Rev. Lett.* **132**, 176702 (2024).
- [5] S. Hayami, Y. Yanagi, and H. Kusunose, Bottom-up design of spin-split and reshaped electronic band structures in antiferromagnets without spin-orbit coupling: Procedure on the basis of augmented multipoles, *Phys. Rev. B* **102**, 144441 (2020).
- [6] I. I. Mazin, K. Koepernik, M. D. Johannes, R. González-Hernández, and L. Smejkal, Prediction of unconventional magnetism in doped FeSb_2 , *Proceedings of the National Academy of Sciences of the United States of America* **118**, e2108924118 (2021).
- [7] R. Jaeschke-Ubierno, V. K. Bharadwaj, T. Jungwirth, L. Smejkal, and J. Sinova, Supercell altermagnets, *Phys. Rev. B* **109**, 094425 (2024).

- [8] R. C. Xiao, D. F. Shao, Y. H. Li, and H. Jiang, Spin photogalvanic effect in two-dimensional collinear antiferromagnets, *npj Quantum Mater.* **6**, 35 (2021).
- [9] T. Osumi, S. Souma, T. Aoyama, K. Yamauchi, A. Honma, K. Nakayama, T. Takahashi, K. Ohgushi, and T. Sato, Observation of a giant band splitting in altermagnetic MnTe, *Phys. Rev. B* **109**, 115102 (2024).
- [10] J. Krempasky, L. Smejkal, S. W. D'Souza, M. Hajlaoui, G. Springholz, K. Uhlířová, F. Alarab, P. C. Constantinou, V. Strocov, D. Usanov *et al.*, Altermagnetic lifting of Kramers spin degeneracy, *Nature* **626**, 517 (2024).
- [11] S. Lee, S. Lee, S. Jung, J. Jung, D. Kim, Y. Lee, B. Seok, J. Kim, B. G. Park, L. Smejkal *et al.*, Broken Kramers Degeneracy in Altermagnetic MnTe, *Phys. Rev. Lett.* **132**, 036702 (2024).
- [12] S. Reimers, L. Odenbreit, L. Smejkal, V. N. Strocov, P. Constantinou, A. B. Hellenes, R. J. Ubiergo, W. H. Campos, V. K. Bharadwaj, A. Chakraborty *et al.*, Direct observation of altermagnetic band splitting in CrSb thin films, *Nat. Commun.* **15**, 2116 (2024).
- [13] N. Nagaosa, J. Sinova, S. Onoda, A. H. MacDonald, and N. P. Ong, Anomalous Hall effect, *Rev. Mod. Phys.* **82**, 1539 (2010).
- [14] Z. X. Feng, X. R. Zhou, L. Smejkal, L. Wu, Z. W. Zhu, H. X. Guo, R. González-Hernández, X. N. Wang, H. Yan, P. X. Qin *et al.*, An anomalous Hall effect in altermagnetic ruthenium dioxide, *Nat. Electron.* **5**, 735 (2022).
- [15] M. Leiviskä, J. Rial, A. Bad'ura, R. L. Seeger, I. Kounta, S. Beckert, D. Kriegner, I. Joumard, E. Schmoranzarová, J. Sinova *et al.*, Anisotropy of the anomalous Hall effect in thin films of the altermagnet candidate Mn₅Si₃, *Phys. Rev. B* **109**, 224430 (2024).
- [16] R. D. Gonzalez Betancourt, J. Zubáć, R. Gonzalez-Hernandez, K. Geishendorf, Z. Sobán, G. Springholz, K. Olejnik, L. Smejkal, J. Sinova, T. Jungwirth *et al.*, Spontaneous Anomalous Hall Effect Arising from an Unconventional Compensated Magnetic Phase in a Semiconductor, *Phys. Rev. Lett.* **130**, 036702 (2023).
- [17] S. W. Cheong and F. T. Huang, Altermagnetism with non-collinear spins, *npj Quantum Mater.* **9**, 13 (2024).
- [18] Q. D. Isaiah Gray, Qi Tian, Michael Chilcote, Matthew Brahlek, Liang Wu, Time-resolved magneto-optical Kerr effect in the altermagnet candidate MnTe, arXiv:2404.05020 (2024).
- [19] H. Y. Ma, M. L. Hu, N. N. Li, J. P. Liu, W. Yao, J. F. Jia, and J. W. Liu, Multifunctional antiferromagnetic materials with giant piezomagnetism and noncollinear spin current, *Nat. Commun.* **12**, 2846 (2021).
- [20] X. C. Mengli Hu, Zhenqiao Huang, Junwei Liu, Catalogue of C-paired spin-valley locking in antiferromagnetic systems, arXiv:2407.02319 (2024).
- [21] L. Smejkal, A. B. Hellenes, R. González-Hernández, J. Sinova, and T. Jungwirth, Giant and Tunneling Magnetoresistance in Unconventional Collinear Antiferromagnets with Nonrelativistic-Momentum, *Phys. Rev. X* **12**, 011028 (2022).
- [22] D. F. Shao, S. H. Zhang, M. Li, C. B. Eom, and E. Y. Tsymbal, Spin-neutral currents for spintronics, *Nat. Commun.* **12**, 7061 (2021).
- [23] H. Bai, L. Han, X. Y. Feng, Y. J. Zhou, R. X. Su, Q. Wang, L. Y. Liao, W. X. Zhu, X. Z. Chen, F. Pan *et al.*, Observation of Spin Splitting Torque in a Collinear Antiferromagnet RuO₂, *Phys. Rev. Lett.* **128**, 197202 (2022).
- [24] J. A. Ouassou, A. Brataas, and J. Linder, dc Josephson Effect in Altermagnets, *Phys. Rev. Lett.* **131**, 076003 (2023).
- [25] M. Milivojevic, M. Orozovic, S. Picozzi, M. Gmitra, and S. Stavaric, Interplay of altermagnetism and weak ferromagnetism in two-dimensional RuF₄, *2D Mater.* **11**, 035025 (2024).
- [26] H. O. Jeschke, M. Shimizu, and I. I. Mazin, CuAg(SO₄)₂: A doubly strongly correlated altermagnetic three-dimensional analog of the parent compounds of high-T_c cuprates, *Phys. Rev. B* **109**, L220412 (2024).
- [27] R. González-Hernández, L. Smejkal, K. Vyborny, Y. Yahagi, J. Sinova, T. Jungwirth, and J. Zelezny, Efficient Electrical Spin Splitter Based on Nonrelativistic Collinear Antiferromagnetism, *Phys. Rev. Lett.* **126**, 127701 (2021).

- [28] A. Bose, N. J. Schreiber, R. Jain, D. F. Shao, H. P. Nair, J. X. Sun, X. S. Zhang, D. A. Muller, E. Y. Tsybal, D. G. Schlom, and D. C. Ralph, Tilted spin current generated by the collinear antiferromagnet ruthenium dioxide, *Nat. Electron.* **5**, 267 (2022).
- [29] Z. H. Zhu, J. Stremper, R. R. Rao, C. A. Occhialini, J. Pellicciari, Y. Choi, T. Kawaguchi, H. You, J. F. Mitchell, Y. Shao-Horn, and R. Comin, Anomalous Antiferromagnetism in Metallic RuO₂ Determined by Resonant X-ray Scattering, *Phys. Rev. Lett.* **122**, 017202 (2019).
- [30] T. Berlijn, P. C. Snijders, O. Delaire, H. D. Zhou, T. A. Maier, H. B. Cao, S. X. Chi, M. Matsuda, Y. Wang, M. R. Koehler *et al.*, Itinerant Antiferromagnetism in RuO₂, *Phys. Rev. Lett.* **118**, 077201 (2017).
- [31] M. Hiraishi, H. Okabe, A. Koda, R. Kadono, T. Muroi, D. Hirai, and Z. Hiroi, Nonmagnetic Ground State in RuO₂ Revealed by Muon Spin Rotation, *Phys. Rev. Lett.* **132**, 166702 (2024).
- [32] L. G.-G. Philipp Keßler, Andreas Suter, Thomas Prokscha, Zaher Salman, Dmitry Khalyavin, Pascal Manuel, Fabio Orlandi, Igor I. Mazin, Roser Valentí, Simon Moser, Absence of magnetic order in RuO₂: insights from μ SR spectroscopy and neutron diffraction, arXiv:2405.10820 (2024).
- [33] Z.-X. Li, X. Wan, and W. Chen, Diagnosing Altermagnetic Phases through Quantum Oscillations, arXiv:2406.04073 (2024).
- [34] D. Shoenberg, *Magnetic Oscillations in Metals*, Cambridge University Press, Cambridge, England, (1984).
- [35] G. Kresse and J. Furthmüller, Efficient iterative schemes for ab initio total-energy calculations using a plane-wave basis set, *Phys. Rev. B* **54**, 11169 (1996).
- [36] J. P. Perdew, K. Burke, and M. Ernzerhof, Generalized gradient approximation made simple, *Phys. Rev. Lett.* **77**, 3865 (1996).
- [37] L. Smejkal, R. González-Hernández, T. Jungwirth, and J. Sinova, Crystal time-reversal symmetry breaking and spontaneous Hall effect in collinear antiferromagnets, *Sci. Adv.* **6**, eaaz8809 (2020).
- [38] X. D. Zhou, W. X. Feng, X. X. Yang, G. Y. Guo, and Y. G. Yao, Crystal chirality magneto-optical effects in collinear antiferromagnets, *Phys. Rev. B* **104**, 024401 (2021).
- [39] A. A. Mostofi, J. R. Yates, Y. S. Lee, I. Souza, D. Vanderbilt, and N. Marzari, wannier90: A tool for obtaining maximally-localised Wannier functions, *Comput. Phys. Commun.* **178**, 685 (2008).
- [40] L. Onsager, Interpretation of the de Haas-van Alphen effect, *The London, Edinburgh, and Dublin Philosophical Magazine and Journal of Science* **43**, 1008 (1952).
- [41] A. Smolyanyuk, I. I. Mazin, L. Garcia-Gassull, and R. Valentí, Fragility of the magnetic order in the prototypical altermagnet RuO₂, *Phys. Rev. B* **109**, 134424 (2024).
- [42] M. H. Cohen and L. M. Falicov, MAGNETIC BREAKDOWN IN CRYSTALS, *Phys. Rev. Lett.* **7**, 231 (1961).
- [43] E. I. Blount, BLOCH ELECTRONS IN A MAGNETIC FIELD, *Physical Review* **126**, 1636 (1962).
- [44] P. A. Goddard and S. J. Blundell, Effect of magnetic breakdown on angle-dependent magnetoresistance in a quasi-two-dimensional metal: An analytically solvable model, *Phys. Rev. Lett.* **77**, 012402 (2008).
- [45] J. Bellissard, M. Gusmão, and T. Ziman, de Haas-van Alphen oscillations and magnetic breakdown: Semiclassical calculation of multiband orbits, *Phys. Rev. Lett.* **57**, 1497 (1998).